Progress In Electromagnetics Research C, Vol. 133, 135–149, 2023

A Shape-Based Approach for Recognition of Hidden Objects Using Microwave Radar Imaging System

Akhilendra Pratap Singh[1, 2, *]

Abstract—Microwave imaging radar systems are often required for the recognition of hidden objects at various job sites. Most existing imaging methods that these systems employ, such as beamforming, diffraction tomography, and compressed sensing, which operate on synthetic aperture radar, produce highly distorted radar images due to the limitation of the frequency range, size of the array, and attenuation during the propagation, and thereby become hard to interpret the description of the object. Several methods explored for the recognition of hidden objects are based on deep neural network models with millions of parameters and high computational costs that render them unusable in portable devices. Moreover, most methods have been evaluated on datasets of microwave radar images of hidden objects with the same relative permittivity, orientation, size, and position. In real-time scenarios, objects may not have similar relative permittivity, orientation, size, and position. Due to variation in the object's relative permittivity, orientation, size, and position, there will also be variation in the reflectivity. Consequently, it is hard to say if those algorithms will be robust in real-world conditions. This paper presents a novel shape-based approach for recognizing hidden objects which combines delay-and-sum beamforming with an artificial neural network. The merit of this proposed method is its ability to simultaneously recognize and reconstruct the object's actual shape from distorted microwave radar images irrespective of any variation in relative permittivity, orientation, size, and position of hidden object. The performance of the developed technique was tested on a dataset of microwave radar images of various hidden objects having different relative permittivities, sizes, orientations, and positions. The proposed method yielded an average reconstruction rate of 91.6%. The proposed method is appropriate for evaluating occluded objects such as utility infrastructure, assets, and weapons detection and interpretation, which have regular shapes and sizes of the cross-section at various construction, archaeological and forensic sites.

1. INTRODUCTION

Nondestructive evaluation of hidden objects using a microwave imaging system is very appealing at various sites. This technology is used for a number of reasons. The first and foremost reason is the ability of microwaves to permeate through the majority of opaque materials. The second reason is the occurrence of dangerous plastic explosives devices that X-ray scanners cannot easily detect because they are essentially devised for metal detection. Due to each object's different permittivity values, microwaves can detect various plastic explosives [1]. The third reason for microwave imaging technology gaining much attention is due to the safety concerns brought on by the non-ionizing nature of microwaves. The reasons mentioned above draw the attention of researchers and lead to exploring the scope of microwave imaging technologies for concealed weapon detection [2], human posture recognition [3],

---

Received 14 April 2023, Accepted 23 May 2023, Scheduled 1 June 2023

[*] Corresponding author: Akhilendra Pratap Singh (akhilendrasing@gmail.com).
[1] School of Engineering and Technology, Maharishi University of Information Technology, Lucknow, U.P., India. [2] Department of Electronics Engineering, Indian Institute of Technology (Banaras Hindu University), Varanasi, U.P., India.
Orchid id: https://orcid.org/0000-0002-2780-1073.

landmine detection [4], mapping building layout [5], static and moving objects detection behind the scene [6, 7], and breast tumor detection [8]. Nowadays, there is much interest among researchers in using microwave imaging technology for exploring hidden objects at various constructions, archaeological and forensic sites [9].

Synthetic aperture radar (SAR) and multiple inputs multiple outputs (MIMO) are the most commonly used microwave imaging system [10–13]. SAR is a cost effect portable microwave imaging system for searching hidden objects [14]. Researchers have presented several imaging methods, such as beamforming, diffraction tomography, and compressed sensing, which operate on synthetic aperture radar [15–18]. However, these imaging algorithms produce highly distorted radar images. Such distortion is caused by the limitation of the frequency range, array size, and attenuation during the propagation in the wall. The radar image formed shows little resemblance to optimal image, making it hard to interpret the object's description. Much work has been done in radar image enhancement; moreover, many developed algorithms still need to consider the real-world constraints faced by operating the hardware devices that run these algorithms. In general, portable microwave imaging systems are lightweight and limited-size devices. These portable hardware devices will have limited memory, computational, and battery power. Many state-of-art algorithms are based on deep neural network (DNN) models with millions of parameters and high computational costs [19, 20]. Applying these methods alleviates insufficient computational power in portable microwave imaging systems that render them unusable in portable devices.

Moreover, most of these algorithms are evaluated on datasets of microwave radar images of objects with similar relative permittivity, orientation, size, and position. Objects in real-time scenarios may not have similar relative permittivity, orientation, size, and position. At various constructions, archaeological and forensic sites, objects of different relative permittivities with variation in orientation, size, and position are present. Due to variations in relative permittivity, orientation, size, and position, there will also be variations in the reflectivity. Consequently, it is hard to say if those algorithms will be robust in real-world conditions. Therefore, there is a need for a technique for the recognition of hidden object irrespective of any change in relative permittivity, orientation, size, and position of hidden objects. For this purpose, a novel shape-based robust approach for recognizing hidden objects which combines delay-and-sum beamforming with an artificial neural network has been proposed that recognizes the actual shape of hidden objects from distorted microwave radar images irrespective of any change in relative permittivity, orientation, size, and object position. Simpler neural network architecture, like single hidden layer dense neural network, can also be explored for hidden object image reconstruction as it can perform as well as deep neural network in terms of image reconstruction fidelity while requiring less computational power and training time [21]. This paper uses a multilayered feedforward neural network incorporating prior information using synthetic training samples. By combining it with delay-and-sum beamforming imaging algorithm, a new possibility of simultaneously recognizing and reconstructing the actual shape of the hidden object has been proposed. The performance of the proposed method was tested on a dataset of microwave images of many basic objects through a brick wall. Compared to the imaging algorithm presented in [16–18], this study suggests a more promising technique to visualize the actual shape of the occluded object with the help of an artificial neural network (ANN) to improve the imaging quality. The developed method accurately recognized the shape of hidden objects of different relative permittivities, orientations, sizes, and positions. The proposed method is appropriate for evaluating hidden or embedded objects such as utility infrastructure detection and interpretation, assets, and weapons with regular cross-section shapes at various construction, archaeological and forensic sites. The structure of the paper is as follows. Section 2 describes the proposed methodology for image reconstruction. Section 3 presents the discussion of experiment results, and Section 4 presents conclusions.

2. PROPOSED METHODOLOGY

This section presents a detailed description of the flowchart as shown in Fig. 1 and the implementation of the proposed framework. The proposed methodology consists of the following stages: data acquisition, image formation by delay-and-sum beamforming, image thresholding, and image improvement using the neural network. The various stages are described further in more detail.

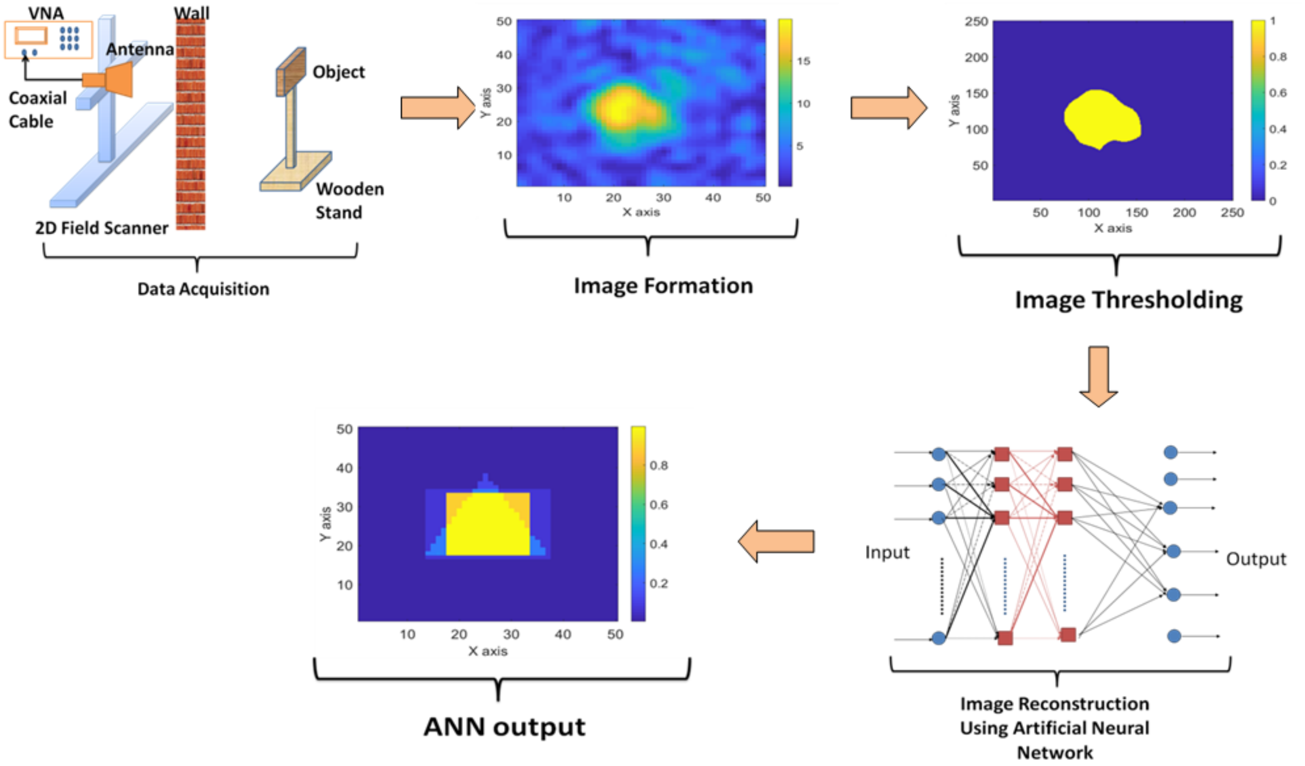

Figure 1. The whole flowchart of the proposed framework.

2.1. Data Acquisition

Figure 1 shows the arrangement of the RF measurement system used for data acquisition placed 220 cm in front of the wall. The measurement system consists of a Vector Network Analyzer (VNA) connected to a horn antenna mounted on a field scanner through a coaxial cable. Fig. 2 shows an actual photograph of the RF measurement setup. The images scene consists of various shapes and sizes of the object with orientations 0°, 45°, and 135° (as described in Table 2) placed on a wooden stand. The data acquisition process involves moving the antenna across 21 × 21 scan points ($M = 21$, $N = 21$) and measuring

Figure 2. Experimental setup of SAR microwave imaging system.

scattering parameter S_{11} for 201 frequency points ($L = 201$) in the frequency band of 3.5–5.5 GHz. The number of frequency steps was set to 201 to retain the 10 MHz frequency step size in order to get the maximum unambiguous range of 15 m. The frequency band of 3.5–5.5 GHz was chosen for imaging as attenuation due to the wall being within the acceptable limit. The acceptable limit for the wall loss is the threshold below which occluded objects cannot be detected. Scattering parameter S_{11} was measured using a 10 kHz intermediate frequency bandwidth (IFBW). Based on the specifications of Anritsu MS2037 VNA, the noise floor level at 10 kHz IFBW is −157 dB. In order to detect the object beyond the wall, the power received must be greater than the noise floor level. The power received can be calculated by radar equation [22]

$$P_r = \frac{P_t G_t G_r \lambda^2 \sigma_t}{(4\pi)^3 R^4 L_c L_w} \approx -124.46\,(\text{dB}) - L_w\,(\text{dB}) \text{ at } 3.42\,\text{m range and center frequency } f = 4.5\,\text{GHz} \quad (1)$$

where,

P_t (Transmitted power) $= -33$ dBW,
$G_t = G_r$ (Gain of antenna) $= 12$ dB,
σ_t (Radar cross-section) $= -20$ dBsm,
$\lambda^2 = -33.6$ dBsm,
$(4\pi)^3 = 33$ dB,
$R^4 = 21.36\,\text{dBm}^4$ at 3.22 m,
$L_c = 2.5$ dB (2-way cable loss),
$L_w =$ wall loss.

Though this equation is a rough approximation, after comparing this equation with noise floor level, the wall loss obtained was $L_w = 32.54$ dB. Thus, 32.54 dB is the maximum attenuation limit of the wall loss, which can be tolerated to detect the object of minimum radar cross-section −20 dBsm. The wall loss of the building wall was measured by the method described in [23] and was found to be 2.3 dB at centre frequency 4.5 GHz, which is less than the maximum attenuation limit of the wall.

2.2. Image Formation Using Delay-and-Sum Beamforming

The image formation consists of the following two stages. The first stage requires wall parameter estimation. The second stage involves the implementation of a delay-and-sum beamforming imaging algorithm with the estimated wall parameters to obtain a focused image of objects.

One of the several significant challenges is to estimate the wall parameters a priori which are essential for compensating the effects of the wall. Researchers have presented several methods to compensate for the effect of the wall. These methods require complex measurement procedures and iterative optimization schemes, which are very computationally intensive [24–26]. In general, portable microwave imaging systems are lightweight and limited-size devices. Applying these methods alleviates insufficient computational power in portable microwave imaging systems [27]. These systems usually form images by using the delay-and-sum beamforming method. The delay-and-sum beamforming method works well with known wall parameters. Ambiguities in wall parameters can smear, blur, and shift away the image of the object from its actual position [27]. Therefore, a time-domain based wall parameter technique has been adopted that works in real-time [28]. The time domain plot of a real building wall, typically constructed with bricks covered by a fine layer of plaster, is shown in Fig. 3. The wall's effective relative permittivity and thickness are estimated using the first two prominent echoes produced by the front and rear walls. The wall's effective relative permittivity and electrical conductivity were estimated by formulating a proper fitness function and minimizing it using an efficient searching technique, a genetic algorithm. Once the wall's effective relative permittivity was estimated, the wall thickness was obtained by Equation (3).

$$F(\varepsilon_w, \sigma) = \min \sum_{K=1}^{M} \left(\frac{P_{R2_K}}{P_{R1_K}} - \left(1 - \left(\frac{\sqrt{\varepsilon_w} - 1}{\sqrt{\varepsilon_w} + 1} \right)^2 \right)^2 \exp^{-\frac{\sigma \eta c \Delta\tau}{\varepsilon_w}} \right)^2 \quad (2)$$

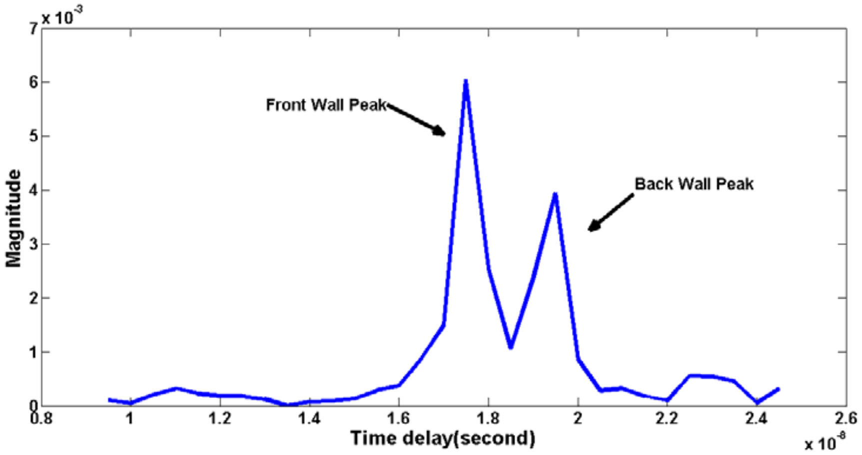

Figure 3. Time domain plot at spatial position $X = 10$, $Y = 10$.

$$d_w = \frac{c\Delta\tau}{2 \times \sqrt{\varepsilon_w}} \tag{3}$$

where,

P_{R2_K} = Power observed at time t_2 due to reflection from the wall-air interface at the backside of the wall at scan point K,

P_{R1_K} = Power observed at time t_1 due to reflection from the air-wall interface at the front side of the wall at scan point K,

ε_w = is the relative permittivity of the dielectric wall,

σ = is the electrical conductivity of the dielectric wall,

σ = is free space intrinsic impedance,

c = is the speed of light,

$\Delta\tau$ = is difference between time t_1 and t_2,

d_w = is the thickness of the dielectric wall,

M = is the number of scan points.

The wall parameters have been computed using the following steps. Step 1: The measured scattering data are converted into equivalent time domain signal using inverse fourier transform. Step 2: Extraction of various parameters, such as P_{R2}, P_{R1}, and $\Delta\tau$, from the time domain signal at each scan point. Step 3: Finally, with the help of Equations (2)–(3), the values of the relative permittivity (ε_w) and the thickness (d_w) of the wall are determined.

After the wall parameters were estimated, acquired frequency domain data in the presence of various objects were processed to produce a 2D-focused radar image of the object at the object plane by applying the delay-and-sum beamforming method. Let the signal in the frequency domain received at each scan point be given as [29]

$$S_{11}\left(x_t, y_t, f_k\right) = a\left(x_b, y_b, z_b\right) \exp\left(-\left(j2\pi f_k \tau_b\right)\right) \tag{4}$$

where $a(x_b, y_b, z_b)$ is the strength of the scattered electric field reflected from the point object, x_b, y_b, z_b the object's location, (x_t, y_t) the scan point location, and τ_b the propagation delay that occurred during signal propagation from the antenna location to the pixel location.

The value of each pixel is estimated by applying propagation phase delays to the acquired frequency domain data for synchronizing the received signal at different antenna positions and summed to compute the value of a pixel at position using Equation (5) [29]

$$I(x_b, y_b, z_b) = \sum_{x_t=1}^{M} \sum_{y_t=1}^{N} \sum_{k=1}^{L} S_{11}(x_t, y_t, f_k) \exp\left(j2\pi f_k \tau_b\right) \tag{5}$$

The object plane was selected by observing the range profile obtained using Equation (6) [23].

$$S(z) = \sum_{k=1}^{L} S_{11}\left(f_k\right) \exp\left(j2\pi f_k(2z + R_{\text{delay}} + 2d_w(\sqrt{\varepsilon_w}))\right) \tag{6}$$

where,

R_{delay} is a delay due to the antenna system;

d_w is the wall thickness;

ε_w is the relative permittivity of wall;

f_k is frequency.

Figure 4 shows the range profile plot of a specific scan point at which reflection due to an object appears. The range profile plot determines the position of z at which reflection due to the object appears as the peak. Fig. 5(a) shows the 2D image of the wooden triangular object (size: 50 cm × 50 cm × 50 cm, orientation: 135°) formed using the delay-and-sum beamform (DS) imaging method.

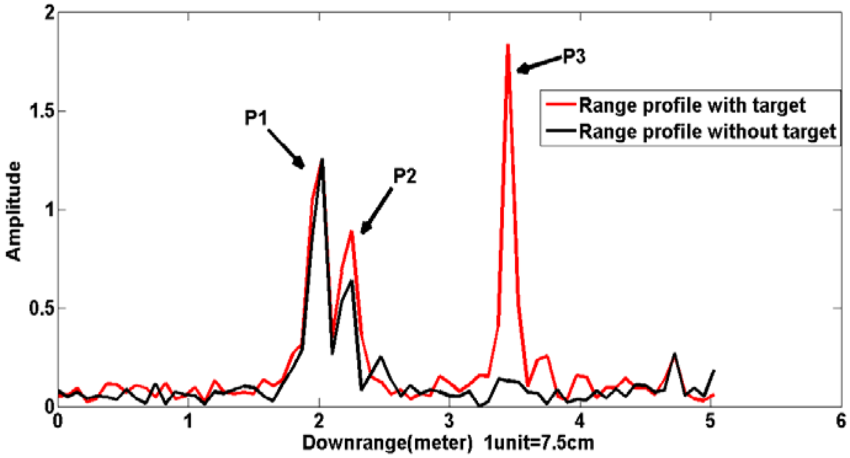

Figure 4. Range profile with and without the object.

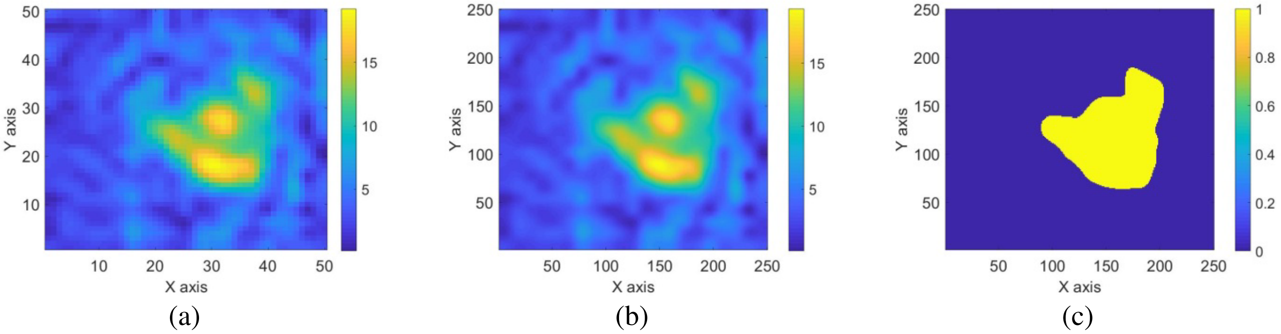

(a) (b) (c)

Figure 5. (a) 2D image of a wooden triangular object formed using delay-and-sum beamform imaging method. (b) Interpolated image. (c) Thresholded image.

2.3. Image Thresholding

The 2D radar image shown in Fig. 5(a) is a low-resolution image of 50 × 50 pixels. Therefore, the size of the images was scaled up to a reasonable size of 250 × 250 pixels using bicubic interpolations, which several authors have used for a long time [30]. The bicubic interpolations method increases the image's size, as shown in Fig. 5(b). The merit of this method is that it preserved the object's shape in the radar image. After that, thresholding is applied to highlight certain image information and remove any unnecessary information, such as the background. The threshold value is computed based on image statistics without histogramming the grey-level values of the image according to a given formula [31]

$$T = \mu + g \times s_d \tag{7}$$

where μ is the mean, s_d the standard deviation, and g the variable whose value is obtained empirically.

2.4. Image Improvement Using Neural Network

The thresholded radar image shown in Fig. 5(c) is highly distorted and has little resemblance to an optical image; thereby, it is hard to interpret it. To overcome this problem, the aim has been to design an ANN-based orientation and scale-invariant image recognition technique that can simultaneously recognize objects and reconstruct the actual shape of objects that appear distorted, irrespective of any variation in orientation, size, and position of the object. The merit of devising an orientation and scale-invariant model is to counter the distortion caused by variations in the orientation, size, and position of the object. The ANN enables us to improve imaging quality by incorporating prior information using training samples. This section first discusses the synthetic data generation and feature extraction process used to create an input data set for training the neural network. It later discusses the neural network model used to recognize and reconstruct the object's actual shape.

2.4.1. Synthetic Data Generation

For study, objects of regular shapes such as rectangle, triangle, and square were considered. Synthetic binary images of objects of size 250×250 pixels were made according to the object's original shape and size as training samples. Devising a rotation and size invariant model requires many training samples of different sizes and orientations to train the ANN. The synthetic images of objects of different orientations and sizes were created with rotation and scaling data augmentation techniques. Like, synthetic data of rectangular shapes of size (50 cm × 30 cm), square shapes of size (30 cm × 30 cm), and the triangular shape of size (35 cm × 35 cm) at orientation 0–330 degrees at the step of 30 degrees have been produced using rotation transformation matrix which is given as [32]

$$\begin{bmatrix} x' \\ y' \end{bmatrix} = \begin{bmatrix} \cos\beta & \sin\beta \\ -\sin\beta & \cos\beta \end{bmatrix} \begin{bmatrix} x \\ y \end{bmatrix} \tag{8}$$

Further, to create the synthetic data samples of various sizes, a morphological dilation technique is used to produce synthetic images of multiple sizes with a structuring matrix [0 1 0; 1 1 1; 0 1 0]. Let C and D be sets of Z^2, the dilation of C by D given as [33]

$$C \oplus D = \left\{ z | (\hat{D})_z \cap C \neq \phi \right\} \tag{9}$$

where C is a binary image, and D is the structuring element.

2.4.2. Feature Extraction

The most popular features for recognizing an object's shape are Fourier descriptors. The main idea is to apply a one-dimensional discrete Fourier transform to the boundary of a two-dimensional shape to extract features from synthetic images. The boundary of each shape denoted by coordinate pair $(x(u), y(u))$ can be treated as complex number which is represented as

$$b\,(u) = x\,(u) + jy\,(u) \tag{10}$$

Equation (11) is the result of applying the discrete Fourier transform to the boundary coordinate pair [34]

$$F\,(v) = \sum_{g=0}^{G-1} b\,(u) \exp\left(-j 2\pi v g / G\right) \tag{11}$$

for $v = 0, 1, 2, ..., V - 1$. The complex coefficient $F(v)$ denotes the Fourier descriptor of the boundary. The only features employed are the magnitudes of the Fourier coefficients. Further, the first 100 coefficients of the Fourier descriptor have been considered, giving relevant information about the object to form a compact feature vector. After extracting the entire feature, it is fed to the artificial neural network for training.

2.4.3. Artificial Neural Network Modelling

For object recognition and its image reconstruction, a three-layer fully connected feedforward neural network is used, which consists of input units, hidden units, and output units [35]. Each synthetic data sample feature vector is first converted into a column vector (100, 1). Accordingly, the feature vectors of all the C training samples is arranged as column vectors to create 2-D input data (100, C). This input data is fed to the input layer for training. Since the aim is to recognize the object and reconstruct its precise image, binary values have been used as the teaching data for the output pattern. These teaching data were 50 × 50 pixels in size and were created based on the shape of their object. After reviewing the input and teaching data, the neural network configured for image reconstruction consists of

Input Units: consist of 100 × 1 nodes equal to the dimension of the feature vector.

Hidden Units: consist of 30 hidden nodes.

Output Units: consist of 50 × 50 output nodes.

2.4.3.1. ***Training ANN Model***

For training, the input data set was randomly divided into training, validation, and testing data in the proportion of 80%, 15%, and 5%, respectively. Fig. 6 shows the structure of the neural network used for training. The output at each node of hidden and output units is defined as [35]

$$o_k = f\left(\sum_j w_{jk} h_i + \theta_k\right) \tag{12}$$

$$h_j = f\left(\sum_i w_{ij} x_i + \theta_j\right) \tag{13}$$

where o_k is the output of unit k; h_j is the output of unit j; w_{jk} is the weight of the connection between unit j and unit k; w_{ij} is the weight of the connection between unit i unit j; θ_k is the bias on unit k; θ_j is the bias on unit j; $\sum\limits_j$ is the summation of every unit j whose output flows from unit j into unit k;

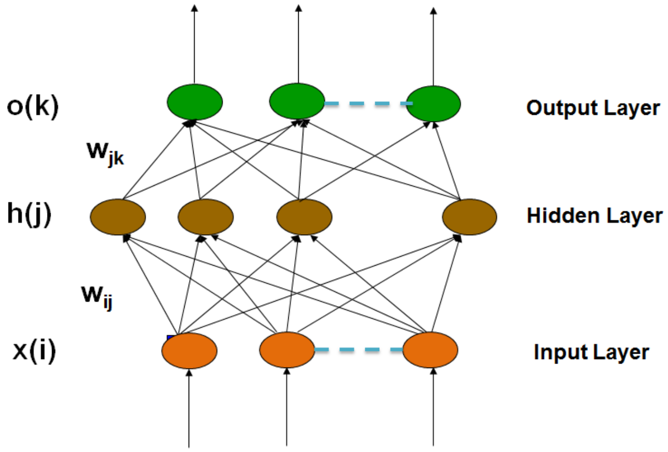

Figure 6. Structure of artificial neural network.

$\sum_i$ is the summation of every unit i whose output flows from unit i into unit j; and $f(n)$ is a sigmoid function which is given by

$$f(n) = \frac{1}{1+e^{-n}} \tag{14}$$

In order to solve the image reconstruction problem, the network's output values must be limited to values between 0 and 1. It was accomplished through the sigmoid transfer function.

The neural network is trained to provide an optimal output when given a collection of m dimensional input patterns $\{x_p = (x_{p1}, x_{p2}, ..., x_{pm});\ p \in P\}$ and a set of n-dimensional desired output patterns $\{o_p = (o_{p1}, o_{p2}, ..., o_{pn});\ p \in P\}$, where P denotes the set of patterns. The network training function Trainscg in Matlab uses a backpropagation learning technique to train the neural network that updates weight and bias values in the path of the steepest descent direction (negative of gradient). Here, the input vector first generates an output vector that is compared to the target vector's output values to determine the value of a predetermined error function that is provided by [35]

$$E = \sum_{p=1}^{P} E_p \tag{15}$$

where

$$E_p = \frac{1}{2} \sum_{k \in \text{output layer}} (o_{pk} - x_{pk})^2 \tag{16}$$

If the error is smaller than a predefined value, then it stops; otherwise adjusts, and the weights and bias of each link lower the error function value based on the steepest descent gradient method, which is given as [35]

$$\Delta w_{jk} = -\eta G_{jk}, \quad \Delta\theta(k) = -\eta G(k) \quad \text{(for output layer)} \tag{17}$$

$$\Delta w_{ij} = -\eta G_{ij}, \quad \Delta\theta(j) = -\eta G(j) \quad \text{(for hidden layer)} \tag{18}$$

Here, η is the small positive constant (learning rate), and G is the gradient which is defined as

$$G = \frac{\partial E}{\partial w} \tag{19}$$

By evaluating the right-hand side of Equations (16) and (17), it follows that

$$\Delta w_{jk} = \eta\delta_k h_j, \quad \Delta\theta(k) = \eta\delta_k \quad \text{(for output layer)} \tag{20}$$

$$\Delta w_{ij} = \eta\delta_j x_i, \quad \Delta\theta(j) = \eta\delta_j \quad \text{(for hidden layer)} \tag{21}$$

where

$$\delta_k = f'(\text{net}_k)(o_{pk} - x_{pk}) \tag{22}$$

$$\delta_j = f'(\text{net}_k) \sum_k w_{jk}\delta_k \tag{23}$$

To speed up the computation, the momentum terms are introduced. This means [35]

$$\Delta w(n+1) = -\eta G + \alpha\Delta w(n) \tag{24}$$

$$\Delta\theta(n+1) = -\eta G + \alpha\Delta\theta(n) \tag{25}$$

where n denotes the nnumber of the learning cycle, and α denotes a small positive value. This process is repeated until the network typically converges to a state where the error is small, which happens after sufficient training cycles.

2.4.3.2. *ANN Training Sample Size Requirements*

Based on the learning curve, the correct number of image data needed for accurate learning was determined [36]. Additionally, the gradient of the learning curve was observed, which shows how much prediction accuracy improves with more training data sets. The basic principle underlying an ANN's learning curve is that greater prediction performance is attained when more samples are used to train the network. This process continues till the learning curve gets to the point of saturation. At this point, the learning rate slows, and the gradient approaches zero, indicating that the training sample amount was sufficient for the ANN to learn. If the learning curve's gradient is less than 10^{-5}, the ANN is thought to have learned the training set. Based on the learning curve, 72 synthetic images of different sizes and orientations, generated with the help of data augmentation techniques, were considered training samples.

3. EXPERIMENTAL RESULTS AND DISCUSSION

This section discusses the performance of combining delay-and-sum beamforming imaging algorithms with trained artificial neural networks and its comparison with different imaging algorithms.

3.1. Result of Combining Delay-and-Sum Beamforming Imaging Algorithm with Trained Artificial Neural Network

The performance of the combining delay-and-sum beamforming imaging algorithm with a trained ANN needs to be tested and evaluated with microwave radar images of various basic shapes of real objects of low and high dielectric constant values. Therefore, an experiment was conducted, and measurement was performed by keeping various shapes and sizes of objects at different orientations and positions (as described in Table 1). The wall was scanned in the XY plane parallel to the wall's surface along the x-axis and y-axis by measuring the back-scattered signals. The data acquired was processed with delay-and-sum beamforming algorithm for 2D radar image formation. Table 2 shows the plot of the 2D radar image of some test samples. The low-resolution 2D radar image of the object is increased using shape-preserving interpolation. The interpolated image is thresholded using Equation (7) to separate the background, and then Fourier feature vectors are extracted from the thresholded image of the object. The extracted feature vector is fed to a trained artificial neural network to reconstruct the actual image of the object. As an example, the result of distorted microwave radar images and their reconstructed images by ANN of some test samples, such as T1 (metallic triangular object, size 50 cm × 50 cm × 50 cm, orientation 0°), T2 (metallic square object, size 30 cm × 30 cm, orientation 0°) placed at 60 cm on the other side of the wall, and T3 (wooden triangular object, size 50 cm × 50 cm × 50 cm, orientation 135°), T4 (wooden rectangular object, size 55 cm × 35 cm, orientation 45°) placed at 120 cm on the other side of the wall, are shown in Table 2. Figs. 7(a)–(d) show actual images of test samples.

The performance of the proposed trained neural network was validated with completely different

Table 1. Detailed information of test objects considered for evaluation.

Shape of Object	Size of Object	Material
Triangle	35 cm × 35 cm × 35 cm	Wood
Triangle	50 cm × 50 cm × 50 cm	Wood
Square	30 cm × 30 cm	Wood
Square	35 cm × 35 cm	Wood
Rectangle	30 cm × 50 cm	Wood
Rectangle	35 cm × 55 cm	Wood
Triangle	35 cm × 35 cm × 35 cm	Metal
Triangle	50 cm × 50 cm × 50 cm	Metal
Square	30 cm × 30 cm	Metal
Square	35 cm × 35 cm	Metal
Rectangle	30 cm × 50 cm	Metal
Rectangle	35 cm × 55 cm	Metal

Table 2. Reconstructed image of occluded objects by trained artificial neural network.

2D DS image of hidden object	Interpolated Image	Thresholded Image	ANN Output
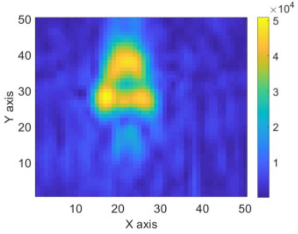 OBJECT ID:T1	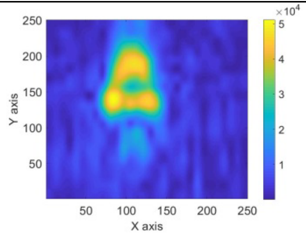	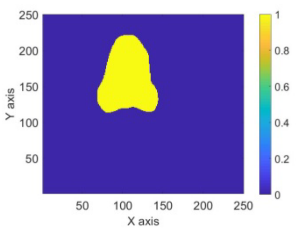	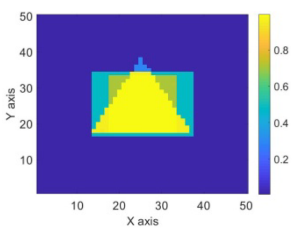
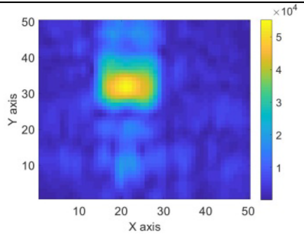 OBJECT ID:T2	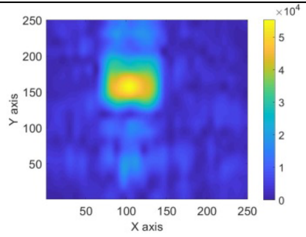	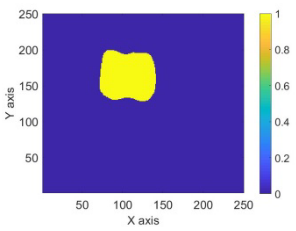	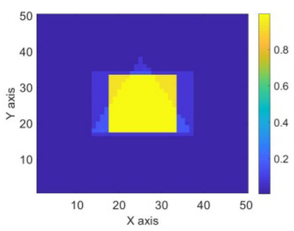
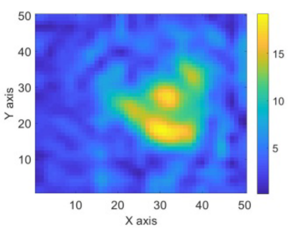 OBJECT ID:T3	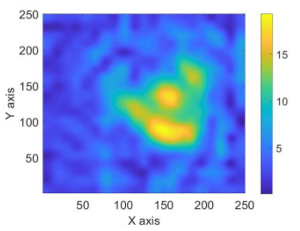	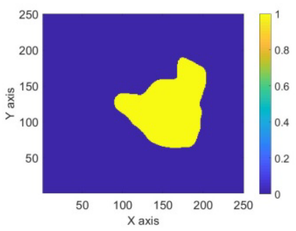	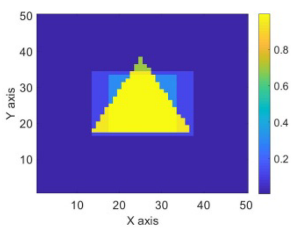
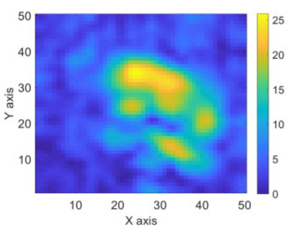 OBJECT ID:T4	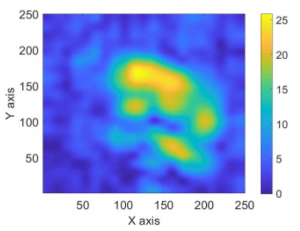	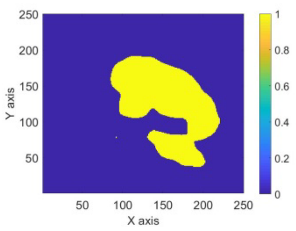	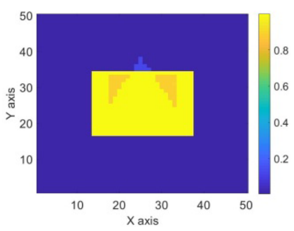

Table 3. Reconstruction rate of ANN for different test samples.

Input	Output	Triangle	Square	Rectangle	Total	Accuracy (%)
	Triangle	11	1	0	12	91.6
	Square	2	10	0	12	83.3
	Rectangle	0	0	12	12	100
					Overall Accuracy	91.6%

test samples (as given in Table 1), which had never before been utilized as input to the network. A confusion matrix for several test samples is shown in Table 3 based on the experimental findings. With these test samples, a 91.6 percent average reconstruction rate was attained. The trained neural network reconstructed the actual shape of concealed objects of different dielectric against any variation in its

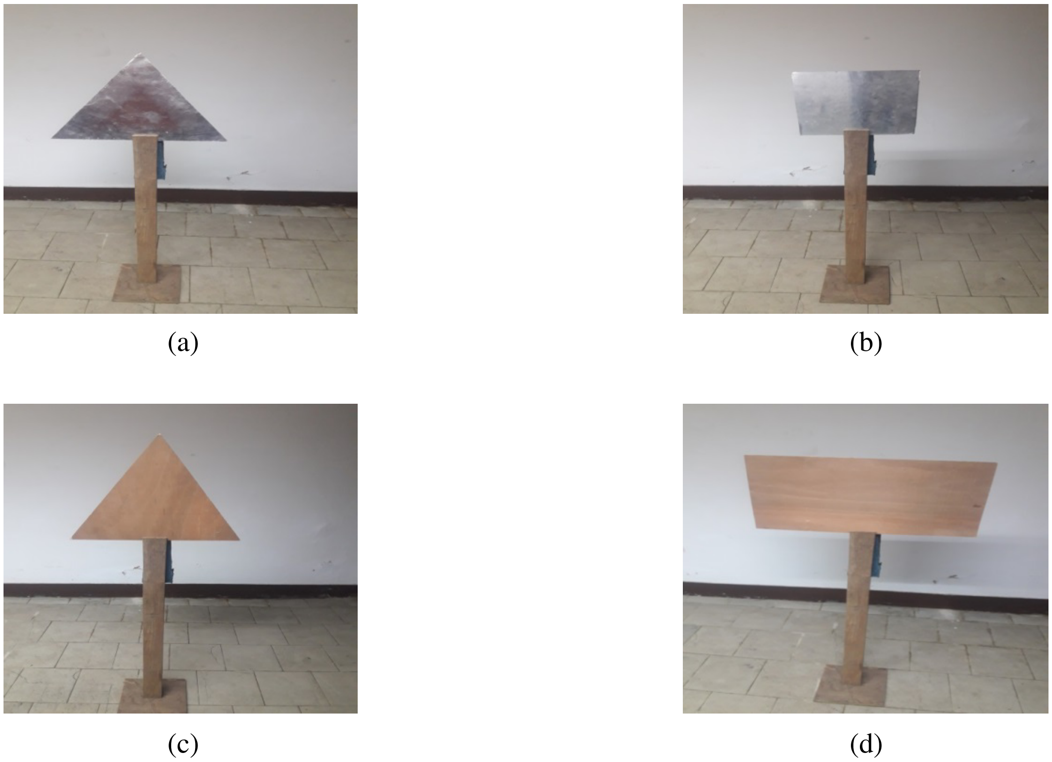
(a) (b) (c) (d)

Figure 7. Actual image of test samples (a) T1, (b) T2, (c) T3, (d) T4.

orientation, size, and position. The 2D radar images reconstructed by the artificial neural network agree with the object's original shapes. Thus, the outcome of trained ANN with distorted radar images of object samples gives satisfactory results with reasonably good performance.

In this paper, experimental results are presented which demonstrate that the proposed method is sufficiently robust in the face of real-world conditions. The majority of real building materials are inhomogeneous. However, if the inhomogeneities are smaller than the range resolution, the wall can be assumed to be homogeneous with effective permittivity [27]. The signal backscattered by such a wall will be similar to that of a homogeneous wall. Furthermore, negligible material dispersion and constant effective permittivity have been assumed in the frequency range of interest. The wall can be lossless or weakly lossy. According to [27], for loss tangent, the real component of the material permittivity dominates in determining the propagation velocity, and the dependency on the loss tangent is minimal. It is obvious that with uniform homogeneous walls best results can be obtained. However, it has been demonstrated that the method can deal with real building walls. Obviously, the proposed method is not appropriate for all possible practical scenarios (e.g., with multilayered or strongly inhomogeneous wall structures).

3.2. Comparison with Different Imaging Algorithms

A comparison analysis is presented in this section to emphasize the importance of the proposed scheme over conventional approaches. The experimental result of the microwave radar image of object T2 produced using the proposed method, along with other imaging algorithms such as synthetic aperture radar [16], diffraction tomography [17], and compressed sensing [18], are shown in Figs. 8(a)–(d). It can be observed that imaging methods proposed in [16–18] produce highly distorted reconstructed images. The radar image formed using these previous methods showed little resemblance to optimal, making it difficult to interpret the object. The neural network approach designed allows us to visualize the original object shape irrespective of any variation in relative permittivity, orientation, size, and position. The experimental result demonstrates the capability of the neural network approach to visualize considered

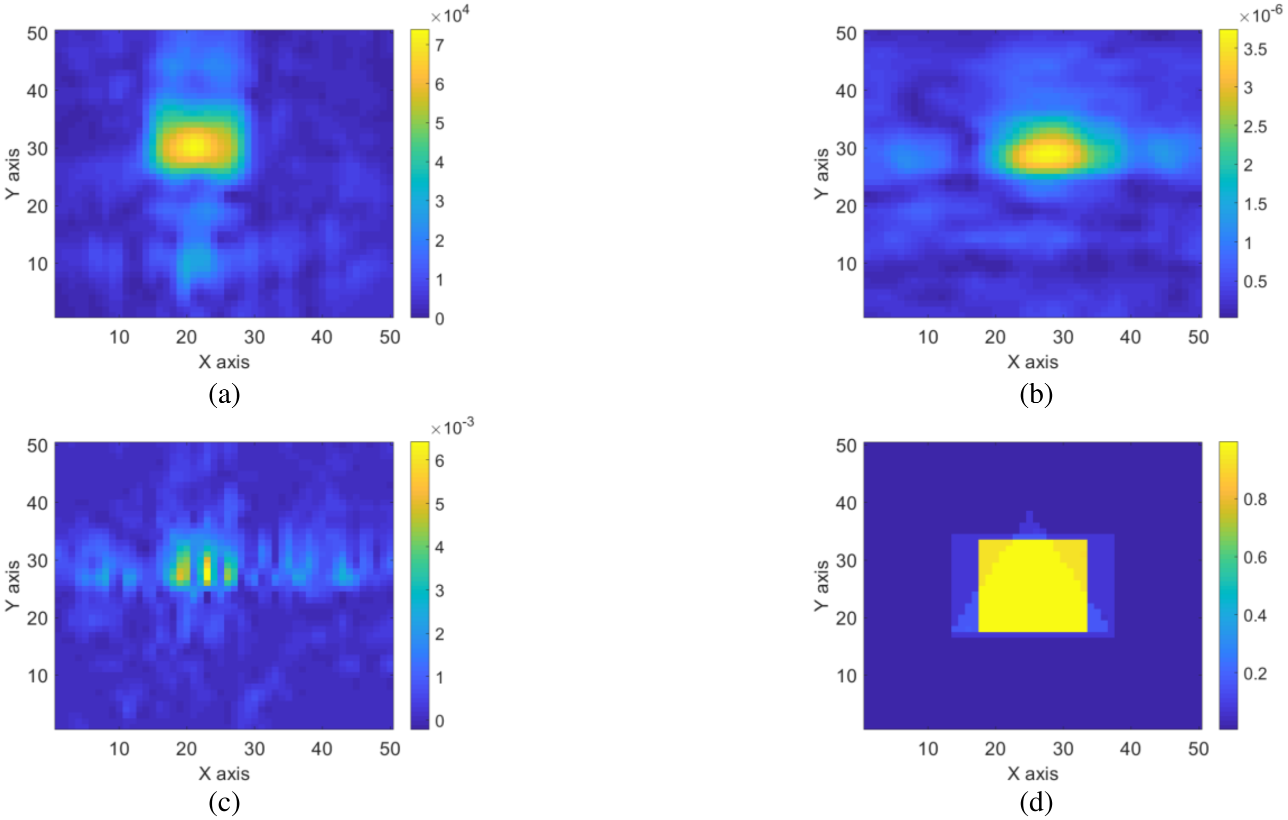

Figure 8. (a) Synthetic aperture radar imaging [16]. (b) Diffraction tomography imaging [17]. (c) Compressed sensing imaging [18]. (d) Proposed method.

regular shape objects. The proposed approach is only appropriate for some possible practical shapes of objects. However, the proposed method can be utilized to evaluate hidden or embedded objects such as utility infrastructure detection and interpretation, assets, and weapons with regular shapes and sizes of the cross-section at various constructions, archaeological and forensic sites, thereby improving the performance of radar systems.

4. CONCLUSION

This paper presents a SAR-based microwave imaging radar system that combines delay-and-sum beamforming imaging method and neural network for recognition of the shape of a hidden object irrespective of any variation in relative permittivity, orientation, size, and position of the hidden object. The performance of the developed technique was evaluated on a dataset of microwave radar images of real hidden objects of various shapes having different relative permittivities, orientations, sizes, and positions. The experimental results show that the proposed technique successfully recognizes and reconstructs actual object's shapes in a heavily cluttered environment. The success rate of reconstruction of distorted radar images was 91.6%. Further, the proposed methodology does not require a separate measurement for estimating wall parameters for image formation. Therefore, it can be used in real-time with different types of walls, such as plywood, brick, and concrete.

REFERENCES

1. Zubair Akhter, A. B. N. and M. J. Akhtar, "Hemisphere lens-loaded Vivaldi antenna for time domain microwave imaging of concealed objects," *Journal of Electromagnetic Waves and Applications*, Vol. 30, 1183–1197, 2016.

2. Tan, W., P. Huang, Z. Huang, Y. Qi, and W. Wang, "Three-dimensional microwave imaging for concealed weapon detection using range stacking technique," *International Journal of Antennas and Propagation*, 2017.
3. Zheng, Z., J. Pan, Z. Ni, C. Shi, S. Ye, and G. Fang, "Human posture reconstruction for through-the-wall radar imaging using convolutional neural networks," *IEEE Geoscience and Remote Sensing Letters*, Vol. 19, 1–5, 2021.
4. Lombardi, F., M. Lualdi, F. Picetti, P. Bestagini, G. Janszen, and L. A. Di Landro, "Ballistic ground penetrating radar equipment for blast-exposed security applications," *Remote Sensing*, Vol. 12, 717, 2020.
5. Chen, B., T. Jin, B. Lu, and Z. Zhou, "Building interior layout reconstruction from through-the-wall radar image using MST-based method," *EURASIP Journal on Advances in Signal Processing*, Vol. 31, 1–9, 2014.
6. Singh, A. P., S. Dwivedi, and P. K. Jain, "A novel application of artificial neural network for recognition of target behind the wall," *Microwave and Optical Technology Letters*, Vol. 62, 152–167, 2020.
7. Singh, V., S. Bhattacharyya, and P. K. Jain, "Micro-Doppler classification of human movements using spectrogram spatial features and support vector machine," *International Journal of RF and Microwave Computer-Aided Engineering*, Vol. 30, e22264, 2020.
8. Celik, A. R. and M. B. Kurt, "Development of an ultra-wideband, stable and high-directive monopole disc antenna for radar-based microwave imaging of breast cancer," *Journal of Microwave Power and Electromagnetic Energy*, Vol. 52, 75–93, 2018.
9. Cicchetti, R., V. Cicchetti, S. Costanzo, P. D'Atanasio, A. Fedeli, M. Pastorino, S. Pisa, E. Pittella, E. Piuzzi, C. Ponti, and A. Randazzo, "A microwave imaging system for the detection of targets hidden behind dielectric walls," *2020 XXXIIIrd General Assembly and Scientific Symposium of the International Union of Radio Science*, 1–4, IEEE, 2020.
10. Nkwari, P. K. M., S. Sinha, and H. C. Ferreira, "Through-the-wall radar imaging: A review," *IETE Technical Review*, Vol. 35, 631–639, 2018.
11. Narayanan, R. M., E. T. Gebhardt, and S. P. Broderick, "Through-wall single and multiple target imaging using MIMO radar," *Electronics*, Vol. 6, 70, 2017.
12. Ralston, T. S., G. L. Charvat, and J. E. Peabody, "Real-time through-wall imaging using an ultrawideband multiple-input multiple-output (MIMO) phased array radar system," *2010 IEEE International Symposium on Phased Array Systems and Technology*, 551–558, IEEE, October 2010.
13. Boudamouz, B., P. Millot, and C. Pichot, "Through the wall radar imaging with MIMO beamforming processing," *2011 Microwaves, Radar and Remote Sensing Symposium*, 251–254, IEEE, August 2011.
14. Laviada, J., A. Arboleya, F. López-Gayarre, and F. Las-Heras, "Broadband synthetic aperture scanning system for three-dimensional through-the-wall inspection," *IEEE Geoscience and Remote Sensing Letters*, Vol. 13, 97–101, 2015.
15. Ahmad, F., Y. Zhang, and M. G. Amin, "Three-dimensional wideband beamforming for imaging through a single wall," *IEEE Geoscience and Remote Sensing Letters*, Vol. 5, 176–179, 2008.
16. Zhang, W. and A. Hoorfar, "Three-dimensional synthetic aperture radar imaging through multilayered walls," *IEEE Transactions on Antennas and Propagation*, Vol. 62, 459–462, 2013.
17. Zhang, W. and A. Hoorfar, "Three-dimensional real-time through-the-wall radar imaging with diffraction tomographic algorithm," *IEEE Transactions on Geoscience and Remote Sensing*, Vol. 51, 4155–4163, 2012.
18. Yoon, Y. S. and M. G. Amin, "Compressed sensing technique for high-resolution radar imaging," *Signal Processing, Sensor Fusion, and Target Recognition XVII, International Society for Optics and Photonics*, Vol. 6968, 69681A, 2008.
19. Song, Y., T. Jin, Y. Dai, Y. Song, and X. Zhou, "Through-wall human pose reconstruction via UWB MIMO radar and 3D CNN," *Remote Sens.*, Vol. 13, 241, 2021.

20. Kılıç, A., İ. Babaoğlu, A. Babalık, and A. Arslan, "Through-wall radar classification of human posture using convolutional neural networks," *International Journal of Antennas and Propagation*, 2019.
21. Zhu, C., E. A. Chan, Y. Wang, W. Peng, R. Guo, B. Zhang, C. Soci, and Y. Chong, "Image reconstruction through a multimode fiber with a simple neural network architecture," *Scientific Reports*, Vol. 11, 1–10, 2021.
22. Skolnik, M., *Introduction to Radar System*, 3rd Edition, McGraw-Hill, New Delhi, 2017.
23. Gaikwad, A. N., D. Singh, and M. J. Nigam, "Application of clutter reduction techniques for detection of metallic and low dielectric target behind the brick wall by stepped frequency continuous wave radar in ultra-wideband range," *IET Radar, Sonar & Navigation*, Vol. 5, 416–425, 2011.
24. Wang, G., M. G. Amin, and Y. Zhang, "New approach for target locations in the presence of wall ambiguities," *IEEE Transactions on Aerospace and Electronic Systems*, Vol. 42, 301–315, 2006.
25. Ahmad, F. and M. G. Amin, "A noncoherent approach to radar localization through unknown walls," *2006 IEEE Conference on Radar*, 2006.
26. Kaushal, S., B. Kumar, and D. Singh, "An autofocusing method for imaging the targets for TWI radar systems with correction of thickness and dielectric constant of wall," *International Journal of Microwave and Wireless Technologies*, Vol. 11, 15–21, 2019.
27. Protiva, P., J. Mrkvica, and J. Machác, "Estimation of wall parameters from time-delay-only through-wall radar measurements," *IEEE Transactions on Antennas and Propagation*, Vol. 59, 4268–4278, 2011.
28. Singh, A. P., S. Dwivedi, and P. K. Jain, "A novel technique for contrast target detection in through-the-wall radar images," *Journal of Electromagnetic Engineering and Sciences*, Vol. 22, No. 3, 202–209, 2022.
29. Tivive, F. H. C., A. Bouzerdoum, and M. G. Amin, "A subspace projection approach for wall clutter mitigation in through-the-wall radar imaging," *IEEE Transactions on Geoscience and Remote Sensing*, Vol. 53, No. 4, 2108–2122, 2014.
30. Sekar, K., V. Duraisamy, and A. M. Remimol, "An approach of image scaling using DWT and bicubic interpolation," *2014 International Conference on Green Computing Communication and Electrical Engineering (ICGCCEE)*, 2014.
31. Singh, A. P., S. Dwivedi, and P. K. Jain, "Development of optimal thresholding technique for shape and size detection for through the wall radar imaging system," *Defence Science Journal*, Vol. 69, 564, 2019.
32. Singh, D., N. K. Choudhary, K. C. Tiwari, and R. Prasad, "Shape recognition of shallow buried metallic objects at X-band using ANN and image analysis techniques," *Progress In Electromagnetics Research B*, Vol. 13, 257–273, 2009.
33. Gonzalez, R. C. and R. E. Woods, *Digital Image Processing Using Matlab*, 2nd Edition, Tata McGraw Hill, New Delhi, 2010.
34. Osowski, S., "Fourier and wavelet descriptors for shape recognition using neural networks — A comparative study," *Pattern Recognition*, Vol. 35, 1949–1957, 2002.
35. Haykin, S., *Neural Network — A Comprehensive Foundation*, 2nd Edition, Pearson Education, New Delhi, 2005.
36. Alwosheel, A., S. van Cranenburgh, and C. G. Chorus, "Is your dataset big enough? Sample size requirements when using artificial neural networks for discrete choice analysis," *Journal of Choice Modelling*, Vol. 28, 167–182, 2018.